Dynamics of two semiconductor lasers coupled by a passive resonator

H. Erzgräber and S. Wieczorek
College of Engineering, Computing and Mathematics, University of Exeter, Exeter EX4 4QF, United Kingdom

B. Krauskopf
Department of Engineering Mathematics, University of Bristol, Bristol BS8 1TR, United Kingdom
(Dated: January 22, 2010)

The stability of two semiconductor lasers that are spatially separated by a passive resonator is analysed using the composite-cavity mode approach. We study the nonlinear interactions of three composite-cavity modes and identify regions of in-phase and out-of-phase laser locking in the parameter plane of the transmission coefficients of the coupling mirrors and the laser length difference. Bifurcation analysis shows that the structure of the locking regions strongly depends on (i) the length of the passive resonator and (ii) the amount of amplitude-phase coupling of the laser field. Specifically, we find a single locking region when the passive resonator and the lasers have comparable lengths and up to three separate locking regions when the passive resonator is much shorter than the lasers. Furthermore, we use the recently developed 0–1 test for chaos to uncover intricate regions of chaotic dynamics that shrink in size and eventually disappear as the passive resonator length becomes comparable to the laser length.

PACS numbers: 02.30.Ks, 05.45.Gg, 02.30.Oz

I. INTRODUCTION

Lasers have been studied for their rich nonlinear dynamical behaviour for several decades [1]. The considerable amount of research on coupled laser systems is stimulated by the recent technological progress as well as fundamental interest. On the one hand, it is now possible to fabricate sophisticated laser structures with several coupled active and passive elements, such as microcavity lasers and lasers embedded into photonic crystals [2–5]. Such structures find many applications, including as optical memory and fast random number generator [6, 7]. On the other hand, coupled lasers become increasingly attractive for studying general synchronization properties and symmetry-breaking effects in coupled nonlinear oscillators [8–12].

Coupled-laser devices usually comprise a passive gap between the lasers that is bounded by parallel reflecting surfaces and can form a passive resonator. Passive resonators occur frequently in optical setups, for example, as Fabry-Perot interferometers or optical filters, and can significantly influence the coupling between lasers. In coupled laser devices the effects of a passive resonator can be eliminated by special optical design. For example, in unidirectionally coupled (optically injected) laser systems optical isolators are used to ensure that light travels from one laser to the other, but there is no coupling in the reverse direction [13–15]. However, even in the absence of optical isolators, effects of a passive resonator are often neglected. The majority of previous studies on bidirectionally coupled semiconductor lasers focused on two different physical situations described by two different types of models. The first type describes coupled lasers that are so close to each other that the passive resonator is excluded from the model. Under weak coupling conditions, such instantaneously coupled lasers can be described by coupled ordinary differential equations [13] that have been studied, for example, in Refs. [13, 16–21]. The second type of model describes coupled lasers separated by a passive gap that is much longer than the laser. Such systems are modelled with coupled delay differential equations [22–28] where the time delay in the coupling term accounts for the distance between the lasers that is much larger than the laser lengths. Neglecting the passive resonator effects in the delay-coupled models is justified by assuming weak coupling between the lasers and, hence, neglecting multiple round-trips within the passive gap [29–31]. Largely unexplored is the intermediate physical situation where lasers are strongly coupled by a passive resonator whose length is comparable to the length of the laser [32, 33].

Here, we study the effects of a passive resonator between two lasers (Fig. 1) on their synchronisation properties and coupling-induced instabilities. We focus on the case where the passive resonator length is comparable to the laser length, and the lasers may be strongly coupled. Under such coupling conditions, neither ordinary nor delay differential equation models are ade-

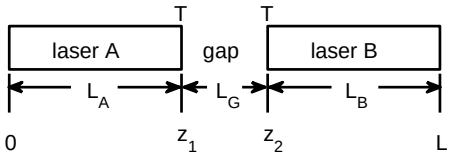

FIG. 1: Sketch of the coupled laser system showing the two lasers of length L_A and L_B that are separated by a passive resonator of length L_G, and the two coupling mirrors with transmission coefficient T.

quate. Alternative modelling approaches include partial differential equations [34, 35] such as, traveling wave models [36], and composite-cavity-mode or supermode models [37, 38]. We use the composite-cavity mode approach [37] to analyse effects of different lengths of the passive resonator ranging from a few microns to hundreds of microns. In this way, we establish a connection between the two widely studied physical situations of instantaneously coupled lasers and delay-coupled lasers.

The nonlinear interactions between composite-cavity modes, which are the eigenmodes of the entire coupled-laser structure, are addressed in two steps. In the first step, we calculate the spatial profiles of the composite-cavity modes and their nonlinear dependence on the geometry of the coupled-laser structure. Specifically, we show that the length of the passive resonator and the transmission coefficient of the coupling mirrors can substantially influence the spatial mode profiles and their frequencies. This results in a nontrivial dependence of the coupling between composite-cavity modes on the length of the passive resonator. In the second step, we use the results of the spatial analysis to study the time evolution of the time-dependent composite-cavity mode amplitudes. The focus is on phase-locking: a continuous wave emission of the coupled-laser system where both lasers emit either in-phase or out-of-phase. Specifically, bifurcation analysis and numerical continuation [39] reveal a complicated structure of the locking region in the plane of the transmission coefficient of the coupling mirrors and the laser length difference. We find that the shape and extent of the different locking regions strongly varies with the length of the passive resonator and the amplitude-phase coupling of the laser (quantified by the linewidth enhancement factor). Furthermore, we apply the recently developed 0-1 test for chaos [40–42] to unveil the intricate structure of chaotic regions where individual lasers exhibit irregular intensity oscillations.

This paper is structured as follows. In Section II we introduce the coupled laser structure. We discuss the composite-cavity modes and their dependence on the passive resonator length and the transmission coefficients of the coupling mirrors. Moreover, we formulate the equations of motion that describe the temporal dynamics of the composite-cavity modes. In Section III we discuss the influence of the passive resonator on the extent and shape of the locking region in the parameter plane of the transmission coefficients of the coupling mirrors and the laser length difference. The analysis is done for two different values of the linewidth enhancement factor namely $\alpha = 0$ and $\alpha = 2$. In Section IV we investigate in more details the effects of the linewidth enhancement factor for two characteristic cases of a small and a large passive gap. In Section V we map out the intricate regions of chaotic dynamics using the 0-1 test for chaos. We conclude with a discussion in Section VI where we stress the connections between our results and other coupled-laser studies.

II. MULTISECTION LASER

Figure 1 shows a sketch of the coupled laser system considered here. Two lasers, A and B, are spatially separated by a passive gap. The gap forms a passive resonator along the longitudinal z-direction in which the laser beam propagates. The individual lasers without coupling are assumed to operate in a single mode with a wavelength of $\lambda_0 = 1\mu$m. The coupling strength between the lasers depends on the transmission coefficient T of the coupling mirrors between the passive gap and the lasers. We assume that both coupling mirrors have identical transmission coefficient and refer to T as *transmission coefficient*. The whole multisection laser is made of semiconductor material. The refractive index of the passive gap $n_r = 3.4$ is equal to the refractive index of the lasers at their (free-running) threshold carrier density. Guided by the symmetry of the system we introduce a *length difference* ΔL between the lasers such that

$$L_A = L_0 + \Delta L\,, \quad L_B = L_0 - \Delta L\,, \tag{1}$$

where (with the exception of Fig. 2), we set $L_0 = 280\mu$m. The size of the passive gap L_G is varied between 5μm and 350μm. We choose L_G such that for $\Delta L = 0$ the gap is in resonance with the free-running lasers.

A. Composite-cavity model

Within the composite-cavity mode approach [37, 43, 44], the spatio-temporal electric field is expanded in terms of spatial eigenmodes $Z_j(z)$ of the entire multisection laser

$$\mathcal{E}(z,t) = \sum_j E_j(t) Z_j(z) + \text{c.c.}\,. \tag{2}$$

For convenience we restrict ourselves to the longitudinal z-direction. The time evolution of the complex-valued electric field amplitude $E_j(t)$ associated with the composite-cavity mode $Z_j(z)$ and the real-valued density of carriers (electron-hole pairs) $N_s(t)$ in laser s are governed by [45],

$$\begin{aligned}\frac{dE_j}{dt} &= -i(\Omega_j - \nu_j)E_j - \gamma E_j \\ &\quad +\gamma \sum_s \Big\{ K^s_{jj}\big(1 + \beta N_s - i\alpha\beta N_s\big)E_j \\ &\quad + \sum_{j'\neq j} K^s_{jj'}\big[1 + \beta N_s - i\alpha\beta(1+N_s)\big]E_{j'} \Big\}\,,\end{aligned} \tag{3}$$

$$\begin{aligned}\frac{dN_s}{dt} &= \Lambda - (N_s + 1) \\ &\quad - \sum_{j,j'} K^s_{jj'}(1+\beta N_s)\text{Re}[E_j E^*_{j'}]\,.\end{aligned} \tag{4}$$

In our example of two single-mode lasers separated by

a passive resonator we consider nonlinear interactions of three composite-cavity modes denoted with $j = \{1, 2, 3\}$. The index $s = \{A, B\}$ refers to the two lasers. Ω_j is the composite-cavity mode frequency and the mode overlap integrals over the active region s are defined as

$$K^s_{jj'} = \frac{n_r}{\mathcal{N}} \int_s Z_j(z) Z_{j'}(z) dz \,, \tag{5}$$

with the normalization constant $\mathcal{N} = n_r^2 L_0$. In the curly bracket in Eq. (3), the terms with K^s_{jj} account for the modal gain and carrier-induced frequency shift of the composite-cavity mode j, and the terms with $K^s_{j'\neq j}$ account for the coupling to the other composite-cavity modes. In particular, the α-parameter quantifies the dependence of the refractive index of semiconductor material, and hence the resonant frequency of the composite-cavity mode, on the carrier density [46]. In nonlinear dynamics terms, α quantifies the coupling between the amplitude and the phase of the electric field inside the multisection laser. Using the same scaling as in Ref. [21] together with parameter values form Table I we get the dimensionless gain parameter $\beta \approx 9.82$ and the ratio of the field and carrier decay rates $\gamma = 10$. The pump rate $\Lambda = 2$ is set to twice the threshold of a free-running laser.

Equations (3)–(4) model the nonlinear dynamics of the coupled laser system in terms of its composite-cavity modes. We are interested in the stability of this system as a function of the laser length difference ΔL, the coupling strength quantified by the transmission coefficient T, the length L_G of the passive resonator, and the amount of amplitude-phase coupling quantified by the α-parameter. As a first step towards the stability analysis of Eqs (3)–(4), we need to compute the spatial profiles $Z_j(z)$ of the composite-cavity modes as a function of ΔL, T, and L_G.

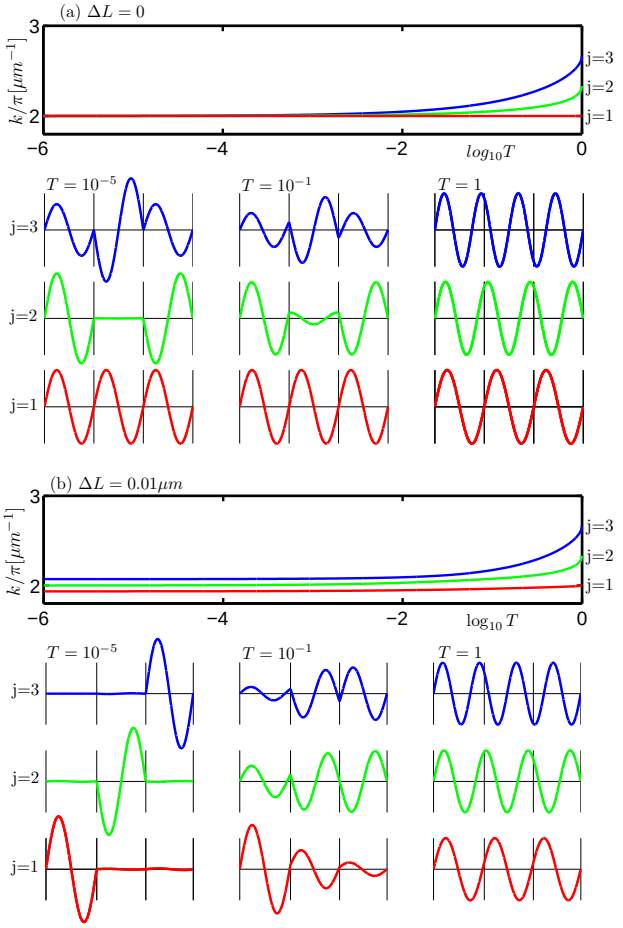

FIG. 2: (Color online) The composite-cavity mode wave number k_j as a function of the transmission coefficient T and examples of composite-cavity mode profiles. $n_r L_0 = n_r L_G = 1\mu$m and $\Delta L = 0$ (a) and $\Delta L = 0.01\mu$m (b).

B. Composite-cavity modes

The composite-cavity modes are calculated assuming that both lasers are at their (free-running) threshold carrier density. They are obtained from Maxwell's equations and appropriate boundary condition. In the longitudinal z-direction the problem reduces to the following Helmholtz equation for the composite-cavity modes $Z_j(z)$

$$\left[\frac{d^2}{dz^2} + n^2(z) k_j\right] Z_j(z) = 0 \,, \tag{6}$$

where $n(z)$ is the space-dependent refractive index and k_j is the composite-cavity mode wave number [47]. Following the idea of Spencer and Lamb [13], the coupling mirrors are modelled as dielectric 'bumps'

$$n(z) = n_r \left[1 + \frac{\eta}{k} \sum_{i=\{1,2\}} \delta(z - z_i)\right] , \tag{7}$$

where $\eta = 2\sqrt{(1-T)/T}$, T is the transmission coefficient of the coupling mirrors, and z_i the position of the ith coupling mirror. Equation (6) is solved together with

symbol	meaning	value
α	linewidth enhancement factor	$0 \leq \alpha \leq 2$
γ_E	cavity decay rate	$1 \times 10^{11} s^{-1}$
γ_N	carrier decay rate	$5 \times 10^{9} s^{-1}$
ξ	differential gain	$2.5 \times 10^{-20} m^2$
Γ	confinement factor	0.1
N_{ts}	carrier density at transparency	$2.0 \times 10^{24} m^{-3}$
n_r	refractive index of the gap	3.4

TABLE I: Laser parameters and their values.

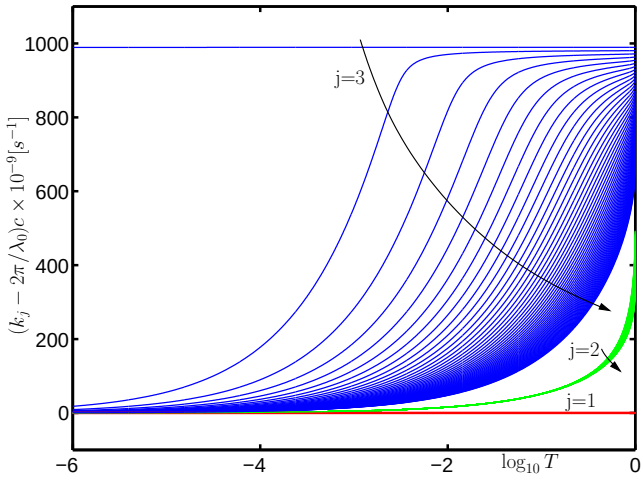

FIG. 3: (Color online) Detuning of the composite-cavity mode frequency Ω_j from the free-running laser frequency $\Omega_0 = 2\pi c/\lambda_0$ as a function of the transmission coefficient T for $L_A = L_B = 280\mu$m and different sizes L_G of the gap; where L_G is increased from 0 to 280μm in 5μm steps in the direction of the arrows.

the following boundary conditions:

$$\begin{aligned} Z(z=0) = Z(z=L) &= 0\,, \\ Z(z=z_i^+) - Z(z=z_i^-) &= 0\,, \\ \frac{d}{dz}Z(z=z_i^+) - \frac{d}{dz}Z(z=z_i^-) &= -\eta k Z(z=z_i)\,, \end{aligned} \tag{8}$$

where $z_i^{\mp}$ denotes the position immediately before $(-)$ and after $(+)$ the coupling mirror at z_i.

We seek solutions in the form of sines and cosines and use the boundary value problem Eqs. (6)–(8) and the orthogonality relation

$$\int_0^L n^2(z) Z_i(z) Z_j(z) dz = \delta_{ij}\mathcal{N} \tag{9}$$

to determine the frequencies and the amplitudes of the composite-cavity modes. For the three composite-cavity modes considered here, the number of symmetric and anti-symmetric composite-cavity modes is determined by the total optical length $n_r(2L_0+L_G)$ of the coupled-laser structure and the wavelength of the solitary laser λ_0. For all values of $n_r(2L_0+L_G)$ considered in this paper we find that composite-cavity modes 1 and 3 are anti-symmetric whereas composite-cavity mode 2 is symmetric. We note that changing $n_r(2L_0 + L_G)$ by half the solitary laser wavelength $\lambda_0/2$ results in composite-cavity modes 1 and 3 being symmetric and composite-cavity mode 2 being anti-symmetric. Figure 2 shows the dependence of the composite-cavity mode wave number k_j and the spatial profiles on the transmission coefficient T for two different cases of ΔL. Figure 2(a) shows the case of identical lasers ($\Delta L = 0$). For transmission coefficient $T = 1$ all three composite-cavity modes become the modes of a single resonator of total length $2L_0+L_G$. They have identical amplitudes in all three sections and their wave number separation is equidistant. As the transmission coefficient is decreased the composite-mode structure changes. While the composite-cavity mode 1 which is in resonance with all three sections remains unaffected, the amplitudes of composite-cavity modes 2 and 3 change as follows. The amplitude of composite-cavity mode 2 becomes smaller in the gap and larger in the lasers, whereas composite-cavity mode 3 shows the opposite behaviour. As T tends to zero, the wave numbers of all three composite-cavity modes become the same but their spatial profiles are quite different. Figure 2(b) shows the case of a laser length difference $\Delta L = 0.01\mu$m. Again, for transmission coefficient $T = 1$ all three composite-cavity modes are the modes of single resonator of total length $2L_0 + L_G$ and have identical amplitudes in all three sections. As T decreases to zero, each composite-cavity mode becomes the mode of a single section, meaning that it has non-zero amplitude only in either of the two lasers or in the passive resonator. As all three sections have different lengths, $L_A > L_G > L_B$, the composite-cavity modes have different wave numbers, $k_3 > k_2 > k_1$ for all $T \in [0, 1]$.

The results in Fig. 2 are obtained for a single wavelength resonators with $n_r L_0 = n_r L_G = 1\mu$m only to simplify illustration of composite-cavity mode profiles. Typical semiconductor lasers are much longer than the wavelength of the light emitted. Therefore, in the remaining sections of this paper we consider a laser length of $L_0 = 280\mu$m. To further understand the effect of the passive resonator, Fig. 3 shows the dependence of the composite-cavity mode frequencies on the passive gap size L_G for $\Delta L = 0$ and $L_0 = 280\mu$m. For each mode $j = \{1, 2, 3\}$ there are 56 different curves corresponding to L_G increasing from 0 to 280μm in 5μm steps as indicated by the arrows. We find that for fixed T the frequency detuning between different composite-cavity modes decreases as L_G in increased. Furthermore, Ω_3 varies more significantly and nonlinearly, compared to Ω_1 and Ω_2, with the transmission coefficient T. In particular, the value of T at which composite-cavity mode 3 comes close to resonance with composite-cavity modes 1 and 2 strongly depends on the the passive resonator length L_G.

Once the lasers are pumped above threshold, each composite-cavity mode receives gain, undergoes a frequency shift, and interacts nonlinearly with all the other modes via the active media in lasers A and B [48, 49]. As all these effects are quantified by the overlap integrals Eq. (5) [37], it is important to understand the dependence of $K^s_{jj'}$ on T, ΔL, and L_G. For the three composite-cavity modes considered here there are eighteen different $K^s_{jj'}$. However, owing to the symmetry of the system, it is sufficient to compute just six of them. Firstly, it is clear from Eq. (5) that $K^s_{jj'} = K^s_{j'j}$. Secondly, the overlap integral $K^B_{jj'}$ in laser B can be obtained from $K^A_{jj'}$ by changing $\Delta L \to -\Delta L$. Figure 4 shows the dependence of the overlap integrals $K^A_{jj'}$ in laser A on T and ΔL for

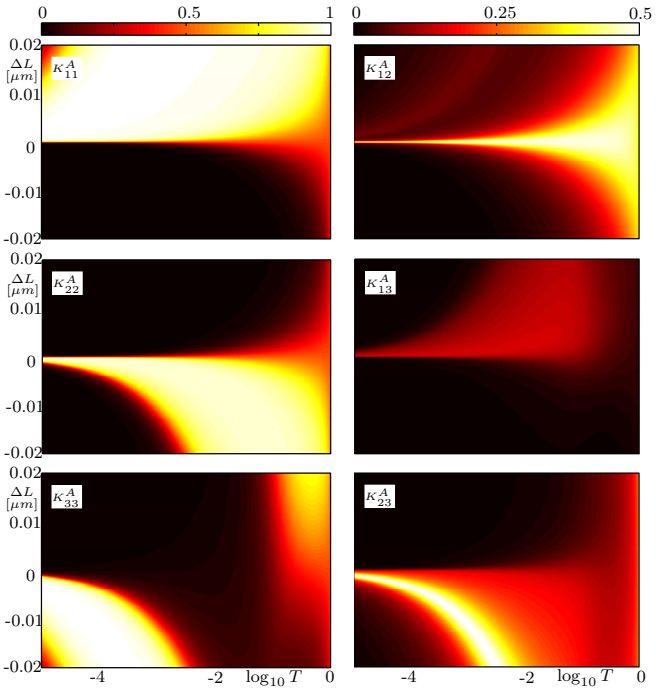

FIG. 4: (Color online) The overlap integrals $K_{jj'}^A$ in laser A as a function of the transmission coefficient T and laser length difference ΔL for $L_0 = 280\mu$m and $L_G = 35\mu$m.

$L_0 = 280\mu$m and $L_G = 35\mu$m. The diagonal terms K_{jj}^A determine the contribution of laser A to the total modal gain and carrier-induced frequency shift of composite-cavity mode j. From Fig. 4 it can be seen that composite-cavity mode 1 is dominant in laser A for positive ΔL over a large range of the transmission coefficient T. In contrast, composite-cavity mode 2 is dominant in laser A for negative ΔL, but only for sufficiently large T. Finally, composite-cavity mode 3 is dominant in laser A for negative ΔL, but only for sufficient small T. The off diagonal terms $K_{j\neq j'}^s$ determine the coupling between composite-cavity modes j and j'. In particular, they depend on the composite-cavity mode amplitudes as well as their relative phases. The overlap integral K_{12}^A between composite-cavity mode 1 and 2 in laser A is large for any T provided the laser length difference $|\Delta L|$ is small enough. The overlap integral K_{13}^A between composite-cavity mode 1 and 3 is noticeably smaller in general. This is because for large T these two composite-cavity modes are not in phase and for small T and for large $|\Delta L|$ composite-cavity mode 3 has vanishing amplitude in laser A. Finally, the overlap integral K_{23}^A between composite-cavity mode 2 and 3 is large only within a narrow band for negative ΔL.

C. Laser Locking

Lasers are locked when they exhibit continuous wave emission with constant intensity and a common optical frequency. Owing to strong optical nonlinearities, lasers can lock to a single frequency even though their individual (un-coupled) frequencies are different. In the composite-cavity model Eqs. (3)–(4) *laser locking* is represented by a single-frequency solution,

$$\begin{aligned} E_j(t) &= |E_j^0| e^{-i(\omega^0 t + \varphi_j^0)}\,, \qquad & j &= \{1,2,3\} \\ N_s(t) &= N_s^0\,, & s &= \{A,B\}\,. \end{aligned} \tag{10}$$

where all nonzero complex-valued modal amplitudes have constant intensities $|E_j^0|^2$, the same optical frequency ω^0, a constant phase-shift φ_j^0, and each laser has a constant carrier density N_s^0. It is useful to distinguish between laser locking with different contributions from different composite-cavity modes as they result in (i) a different phase relation between the two lasers, and (ii) a different spatial field distribution within the multisection laser device. On the one hand, locking can be dominated by a single composite-cavity mode with all the other composite-cavity modes having negligible amplitudes $|E_j^0|$. On the other hand, locking can be obtained when more than one composite-cavity modes have nonzero amplitudes $|E_j^0|$ but are phase locked to a common frequency ω^0.

In the following section, we study stability of the locked solution Eqs. (10) in the parameter plane of the transmission coefficient T, which quantifies the coupling strength between the lasers, and the laser length difference ΔL, which quantifies the frequency detuning between the lasers. More specifically, locking regions of Eqs. (3)–(4) are bounded in the $(T, \Delta L)$ plane by Hopf (H) and saddle-node (S) bifurcation curves. The thick parts of these bifurcation curves mark the loss of stability of the locked solution Eqs. (10). Crossing these bifurcation curves results in different locking-unlocking transitions. In the case of a Hopf bifurcation, the locked solution Eqs. (10) loses stability and in the case of a saddle-node bifurcation, the locked solution Eqs. (10) may appear or disappear. We use the method of numerical continuation [39] to compute these two bifurcations. In this way, we provide a systematic study of the locking regions and reveal interesting effects of the passive gap size L_G and the α-parameter. Outside the locking regions, the system can exhibit periodic composite-cavity mode beating, quasi-periodic oscillations, or even chaos.

III. INFLUENCE OF THE GAP

Changing the passive resonator length L_G affects the composite-cavity mode frequencies Ω_j (Fig. 3) as well as the overlap integrals $K_{jj'}^s$ that quantify the modal gains, carrier-induced frequency shifts, and the coupling strength between composite-cavity modes. Hence,

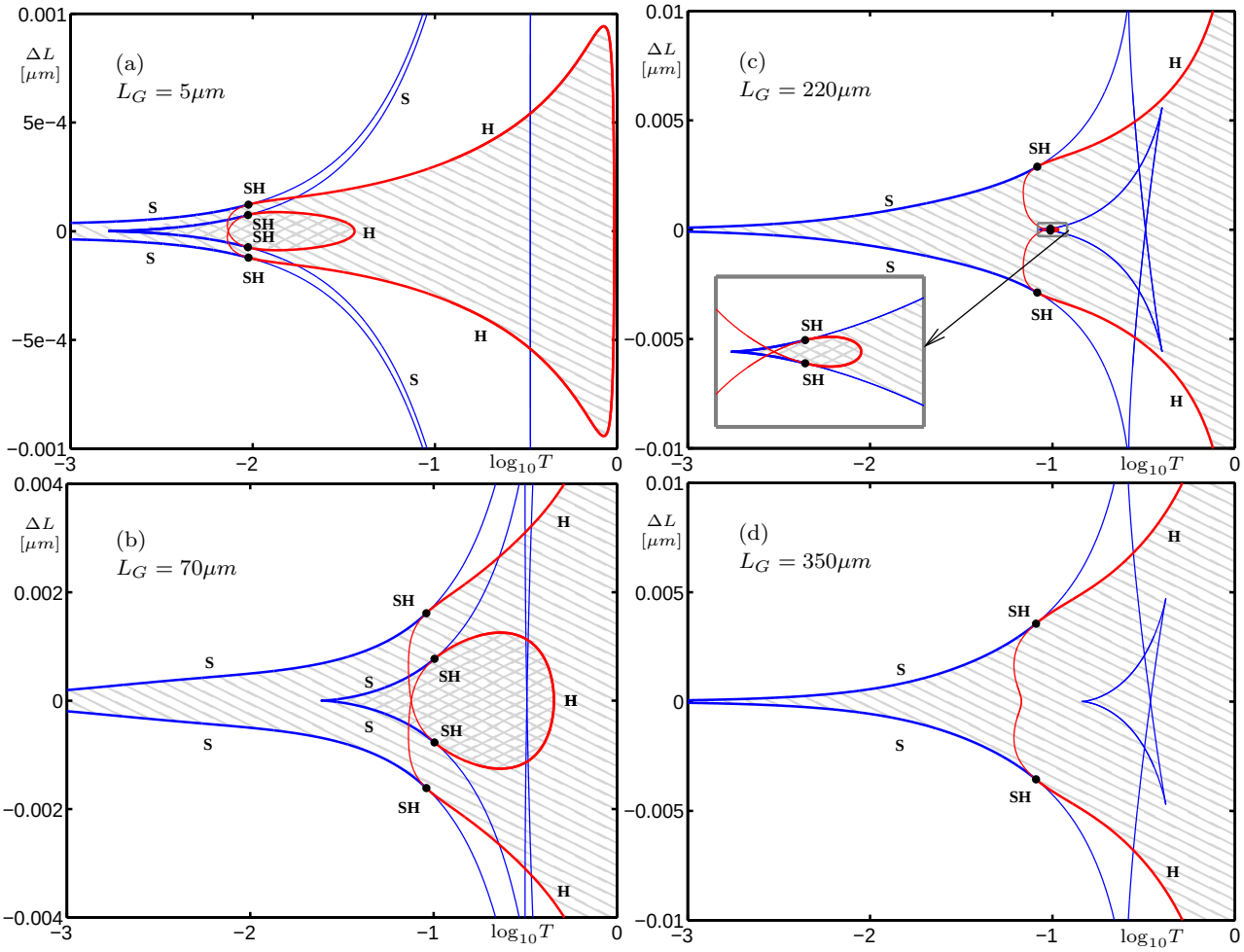

FIG. 5: (Color online) Bifurcation diagrams for in the $(T, \Delta L)$ plane for different sizes of the gap L_G and fixed $\alpha = 0$. Left inclined hatching indicates cw-operation in mode 2, right inclined hatching cw-operation of mode 1, crossed hatching bistability of both modes. Curves are saddle-node (S) and Hopf (H) bifurcations; black dots are codimension-two saddle-node Hopf (SH) and double Hopf (HH) points. The inset shows an enlarged view around certain codimension-two bifurcations as indicated by the arrow.

one expects strong modifications to the locked solutions Eqs. (10) and their stability when varying L_G. This section identifies qualitative changes of the stable locking region arising from increasing L_G. In this way, it extends the studies of lasers with instantaneous coupling [16–21] to the case of a non-negligible gap size.

A. Zero amplitude-phase coupling

First, we consider the case of $\alpha = 0$, that is zero coupling between the amplitude and the phase of the electric field inside the lasers. (This is the case, for example, in gas, crystal, and quantum dot semiconductor lasers.) Figure 5 shows the dependence of the locking region in the $(T, \Delta L)$ plane on the size L_G of the passive gap. The left inclined hatching indicates stable locking (10) dominated by composite-cavity mode 2. Since this mode is symmetric, the two lasers emit in-phase. In contrast, the right inclined hatching indicates stable locking (10) dominated by composite-cavity mode 1. Composite-cavity mode 1 is anti-symmetric, meaning that the two lasers emit out-of-phase. For small values of the transmission coefficient T the locking region is bounded by saddle-node (S) bifurcations and for larger T it is bounded by Hopf (H) bifurcations. Codimension-two saddle-node Hopf (SH) points mark the change in the type of the locking boundary. The two striking features of the stable locking in Fig. 5 are sensitivity to the laser length difference and bistability. For a relatively small gap of $L_G = 5\mu$m [Fig. 5(a)], the (larger) locking region dominated by composite-cavity mode 1 extends over all values of T. The (smaller) locking region dominated by composite-cavity mode 2 extends only over a short inter-

val of $T \sim 10^{-2}$. For such a small gap, already a sub-nanometer difference in the lasers length, corresponding to a laser frequency detuning of GHz, makes it impossible for the lasers to lock. However, as L_G increases, the composite-cavity mode 2 dominated locking region expands in ΔL by a factor of ten [compare the range of ΔL in panels (a) and (d) in Fig. 5]. Bistability between composite-cavity mode 1 and 2 dominated locking is indicated by the cross hatching. As the passive gap size increases, the bistable locking region expands in ΔL and moves toward larger T [compare panels (a) and (b) in Fig. 5]. However, it then starts shrinking and eventually disappears when L_G becomes comparable to L_0 [compare panels (c) and (d) in Fig. 5]. The bistable locking region disappears via a codimension-three pitchfork-Hopf bifurcation where the two (codimension-two) saddle-node Hopf points come together at the cusp of the saddle-node curve. The inset in Fig. 5(c) shows an enlarged view of the bistable region just before it disappears. For L_G comparable to L_0 we find only a single and monostable locking region in the $(T, \Delta L)$ plane [Fig. 5(d)].

When $\alpha = 0$ there are no frequency shifts with varying carrier density and the coupling terms in Eq (3) simplify noticeably. A comparison with Figs. 3 and 4 shows that the locking regions can be explained by different modal gains and different coupling coefficients between composite-cavity modes. In particular, the larger locking region dominated by composite-cavity mode 2 and the smaller locking region dominated by composite-cavity mode 1 correlate well with the higher modal gain of mode 2 near the resonance $\Delta L = 0$. Furthermore, a lack of a locking region that is dominated by composite-cavity mode 3 is a result of vanishing modal gain and weak coupling to composite-cavity modes 1 and 2 near $\Delta L = 0$.

B. Non-zero amplitude-phase coupling

Coupling between the amplitude and the phase of the electric field is characteristic of most semiconductor lasers. It causes frequency shifts of the composite-cavity modes with varying carrier densities in lasers A and B, and noticeably complicates the mode-coupling mechanisms; see Eqs. (3) and [21, 48]. This section presents the effects of L_G on the structure of the locking regions in the (T, Δ) parameter plane for $\alpha = 2$.

Again, in Fig. 6 different hatching indicate different stable locked solutions Eqs. (10). The left inclined locking region is dominated by composite-cavity mode 2 and the right inclined locking region is dominated by composite-cavity mode 1. The two striking features of stable locking are a much more complex structure of the locking regions and the lack of bistability. For a relatively small gap of $L_G = 5\mu$m we find three detached locking regions [Fig. 6(a)]. At large T (strong laser coupling) there is a small locking region dominated by the anti-symmetric composite-cavity mode 1. This locking region is bounded by a looped Hopf (H) curve to the right and a saddle-node (S) curve with a cusp point to the left. Changes in the type of the locking boundary are marked by codimension-two saddle-node Hopf (SH) points, as can be seen in the inset of Fig. 6(a). For intermediate values of T there is a large locking region dominated by the symmetric composite-cavity mode 2 (left inclined). This locking region is bounded by different Hopf curves towards increasing and decreasing T, as well as by saddle-node curves toward increasing $|\Delta L|$. Changes in the type of the locking boundary are marked by codimension-two saddle-node Hopf (SH) points and double Hopf (HH) points. Finally, for very small T (weak laser coupling) there is a locking region with contributions from composite-cavity modes 1 and 3, which are both locked to a common frequency ω^0. This locking region is bounded by a single Hopf curve toward increasing T and saddle-node curves towards increasing $|\Delta L|$. Changes in the type of the locking boundary are indicated by two saddle-node Hopf points.

As the gap L_G between the lasers is increased, the locking regions undergo several qualitative and quantitative changes. These changes indicate that the coupled-laser system is more sensitive to varying L_G for non-zero α. The qualitative changes can be described as transitions through various codimension-three bifurcation points, details of which are beyond the scope of this paper. To give an example, Fig. 6(b) shows the locking region structure for $L_G = 10\mu$m that is a result of such transitions. Compared to panel (a), the locking region at intermediate T is much smaller and bounded only by a single Hopf curve. In contrast, the locking region at low T is noticeably expanded. The inset in Fig. 6(b) shows an enlarged view around the codimension-two points on the boundary of this locking region. There are two Hopf curves that cross in a double Hopf point (HH). These different Hopf bifurcations are associated with unlocking transitions to intensity oscillations with different frequency. In addition, there are two saddle-node-Hopf points (SH) that are also present in panel (a). As L_G increases from 5μm to 10μm, the two saddle-node Hopf points swap their relative position on the saddle-node curve. As a result of the swap, a double Hopf (HH) point emerges on the locking boundary via degenerate saddle-node-Hopf bifurcation.

In Fig. 6(c) for $L_G = 70\mu$m, there are just two separate locking regions as the third (middle) locking region completely disappeared. The larger locking region results from the expansion of the locking region found at weak coupling in panel (b). The codimension-two points indicating the change in the type of its boundary moved outside of the parameter region displayed in Fig. 6(c). In particular, one saddle-node Hopf point moved to even smaller T and the double Hopf point moved to larger $|\Delta L|$. The smaller locking region at large T expanded in size but did not undergo any qualitative changes between panels (b) and (c). When L_G is increased further, the locking region at strong coupling also disappears [Fig. 6(d)]. For $L_G = 350\mu$m, this leaves just a single

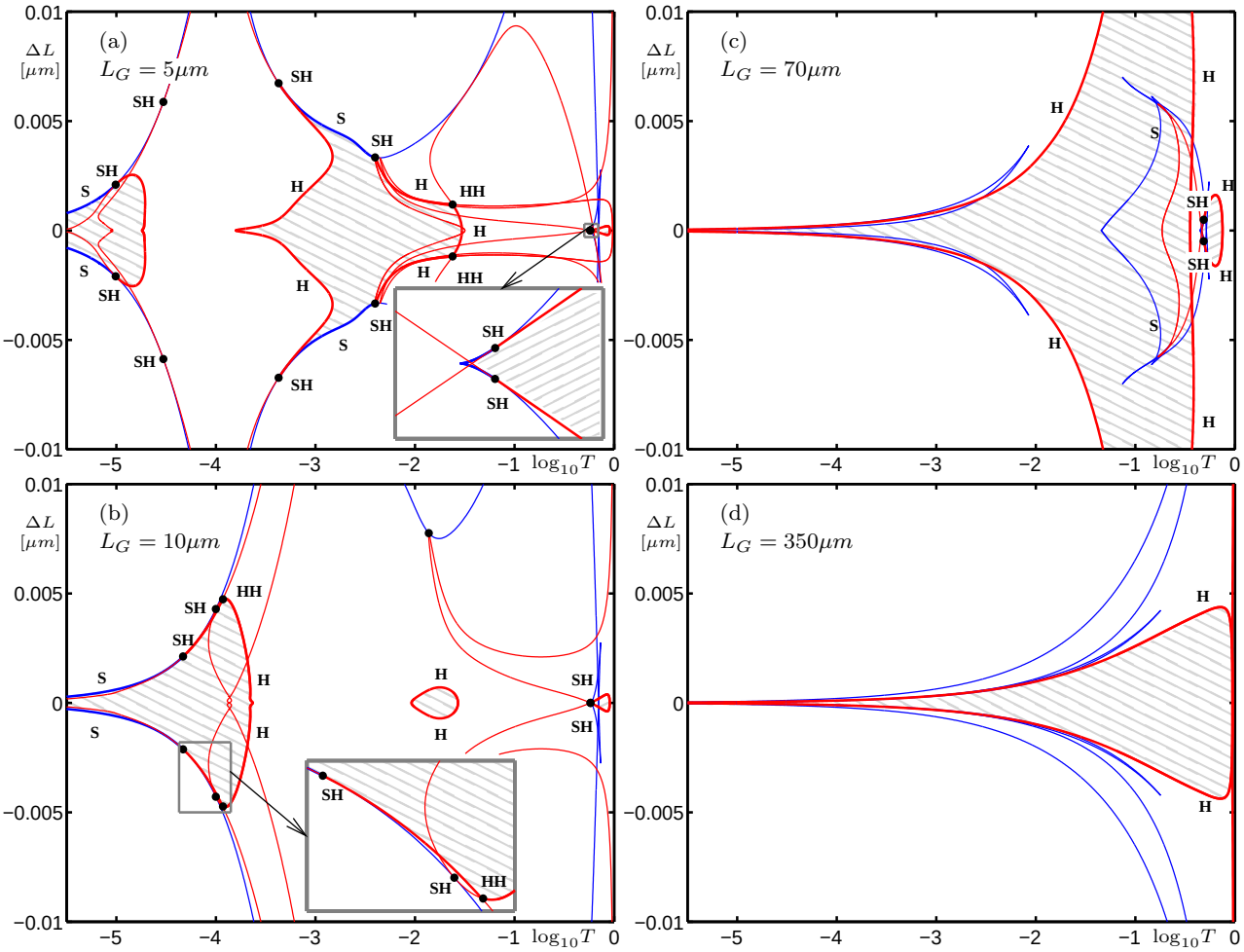

FIG. 6: (Color online) Bifurcation diagrams for in the $(T, \Delta L)$ plane for different sizes of the gap L_G and fixed $\alpha = 2$. Left inclined hatching indicates cw-operation in mode 2, right inclined hatching cw-operation of mode 1, crossed hatching bistability of both modes. Curves are saddle-node (S) and Hopf (H) bifurcations. Black dots are codimension-two saddle-node Hopf (SH) and double Hopf (HH) points. The insets show enlarged views around certain codimension-two bifurcations as indicated by the arrows.

locking region in the $(T, \Delta L)$ plane that is bounded by a Hopf bifurcation.

To illustrate the contributions of different composite-cavity modes to the dynamics explicitly, we plot one-parameter bifurcation diagrams of the modal intensities $|E_{1,2,3}|^2$ in Figs. 7 and 8. In these diagrams, for each fixed ΔL we show the minima and maxima extracted from the time evolution of $|E_{1,2,3}|^2$. Hence, a single dot indicates constant intensity emission or locking, two or more distinct dots indicate periodic oscillations, and many closely spaced dots indicate quasi-periodic or chaotic oscillations.

Figure 7 shows the case of a small gap with $L_G = 5\mu$m, $\alpha = 2$, and should be compared with Fig. 6 (a). Figure 7(a)–(c) shows the case of strong laser coupling with the transmission coefficient $T = 10^{-0.017}$. Within the small locking region around $\Delta L = 0$ only (anti-symmetric) composite-cavity mode 1 has non-negligible intensity. As the laser length difference $|\Delta L|$ is increased, locking is lost via a Hopf bifurcation. At the bifurcation, there is an abrupt switch from composite-cavity mode 1 to composite-cavity mode 3. Just past the bifurcation, composite-cavity mode 3 is the only mode with non-negligible intensity. It oscillates periodically but with such a small amplitude that in an experiment this could still resemble locking. As $|\Delta L|$ is further increased, the intensity of composite-cavity mode 3 gradually decreases, whereas the intensity of composite-cavity modes 1 and 2 gradually increases. The contribution from composite-cavity mode 2 is smaller compared to the other modes. Figure 7(d)–(e) shows the case of intermediate laser coupling with $T = 10^{-3.3}$. Now, the locking region around $\Delta L = 0$ is dominated by composite-cavity mode 2. As $|\Delta L|$ is increased, locking is lost via a saddle-node bifurcation. Past the bifurcation, the laser system exhibits chaotic intensity oscillations interrupted by small win-

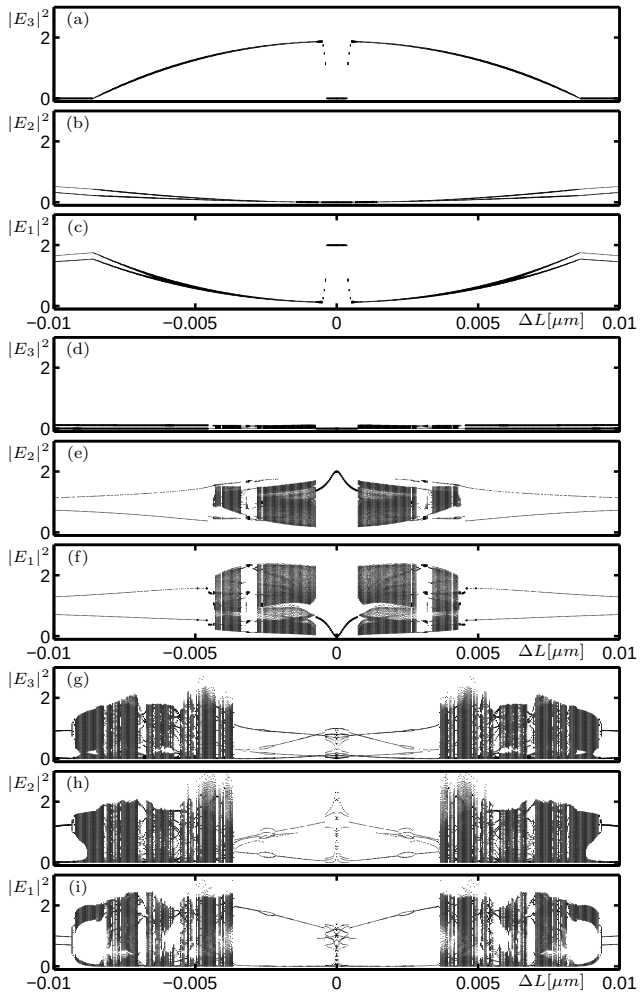

FIG. 7: One-parameter bifurcation diagram for $\alpha = 2$ and $L_G = 5\mu$m. Plotted are the extrema of the modal intensities $|E_{j=1,2,3}|^2$ as a function of the laser length difference ΔL for transmission coefficient $T = 10^{-0.07}$ (a)–(c), $T = 10^{-3.3}$ (d)–(f), and $T = 10^{-4.5}$ (g)–(i)

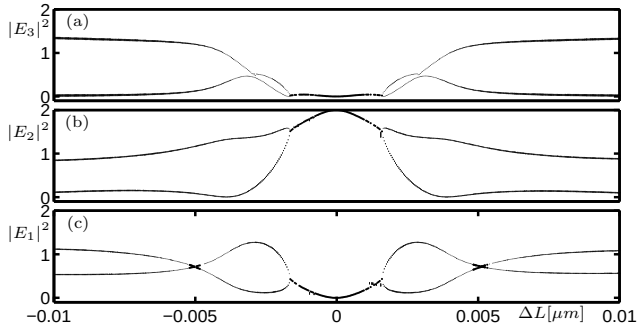

FIG. 8: One-parameter bifurcation diagram for $\alpha = 2$ and $L_G = 350\mu$m. Plotted are the extrema of the modal intensities $|E_{j=1,2,3}|^2$ as a function of the laser length difference ΔL for transmission coefficient $T = 10^{-2}$ (a)–(c).

dows of periodic oscillations. For sufficient large $|\Delta L|$, there is a transition to periodic intensity oscillations. The contribution from composite-cavity mode 3 is much smaller compared to the two other modes over the considered interval of ΔL. Figure 7(g)–(i) shows the case of weak laser coupling with $T = 10^{-4.5}$. Now, the system exhibits intensity oscillation with comparable contributions from all three composite-cavity modes over the entire interval of ΔL. We find periodic intensity oscillations at $|\Delta L| \sim 0$, an onset of chaotic intensity oscillations at around $|\Delta L| = 0.004$, and periodic intensity oscillations again for $|\Delta L| > 0.009$.

Figure 8 shows the case of a large gap with $L_G = 350\mu$m, $\alpha = 2$, $T = 10^{-2}$, and should be compared with Figure 6 (d). The locking region at $|\Delta L| \sim 0$ is dominated by composite-cavity mode 2. When $|\Delta L|$ is increased, the contribution of composite-cavity mode 2 to locking slightly decreases, the contribution of composite-cavity mode 1 slightly increases, and composite-cavity mode 3 remains negligible. After locking is lost via a Hopf bifurcation, all three composite-cavity modes exhibit periodic intensity oscillations with non-negligible amplitudes.

Unlike for $\alpha = 0$, the locking regions uncovered for $\alpha = 2$ cannot be understood just in simple terms of losses and modal gain as indicated by the overlap integrals $K_{jj'}$. Rather, to explain the intricate structure of stable locking, one has to invoke the additional effects of carrier-induced frequency shifts and mode-coupling mechanisms including additional gain suppression owing to nonzero α.

IV. INFLUENCE OF AMPLITUDE-PHASE COUPLING

Section III revealed drastically different dependencies of the locking region on the gap size L_G for $\alpha = 0$ and $\alpha = 2$. This section discusses in more detail the qualitative changes of the locking region as the α-parameter increases from 0 to 2 for two representative cases of small $L_G = 35\mu$m and large $L_G = 280\mu$m gap size.

A. Small gap

Figure 9 shows the transformation of the locking regions for $L_G = 35\mu m \ll L_0$ with increasing α. For $\alpha = 0$ [Fig. 9(a)], we recover qualitatively the same result as in Fig. 5(a). There is a single uninterrupted locking region that extends from weak to strong laser coupling and involves bistability. Stable locking dominated by the symmetric (antisymmetric) composite-cavity mode 2 (1) is indicated by left (right) inclined hatching, and bistability is found in the cross-hatched area. Locking is lost via saddle-node (S) or Hopf (H) bifurcation and saddle-node Hopf (SH) points mark the changes in the type of the locking boundary.

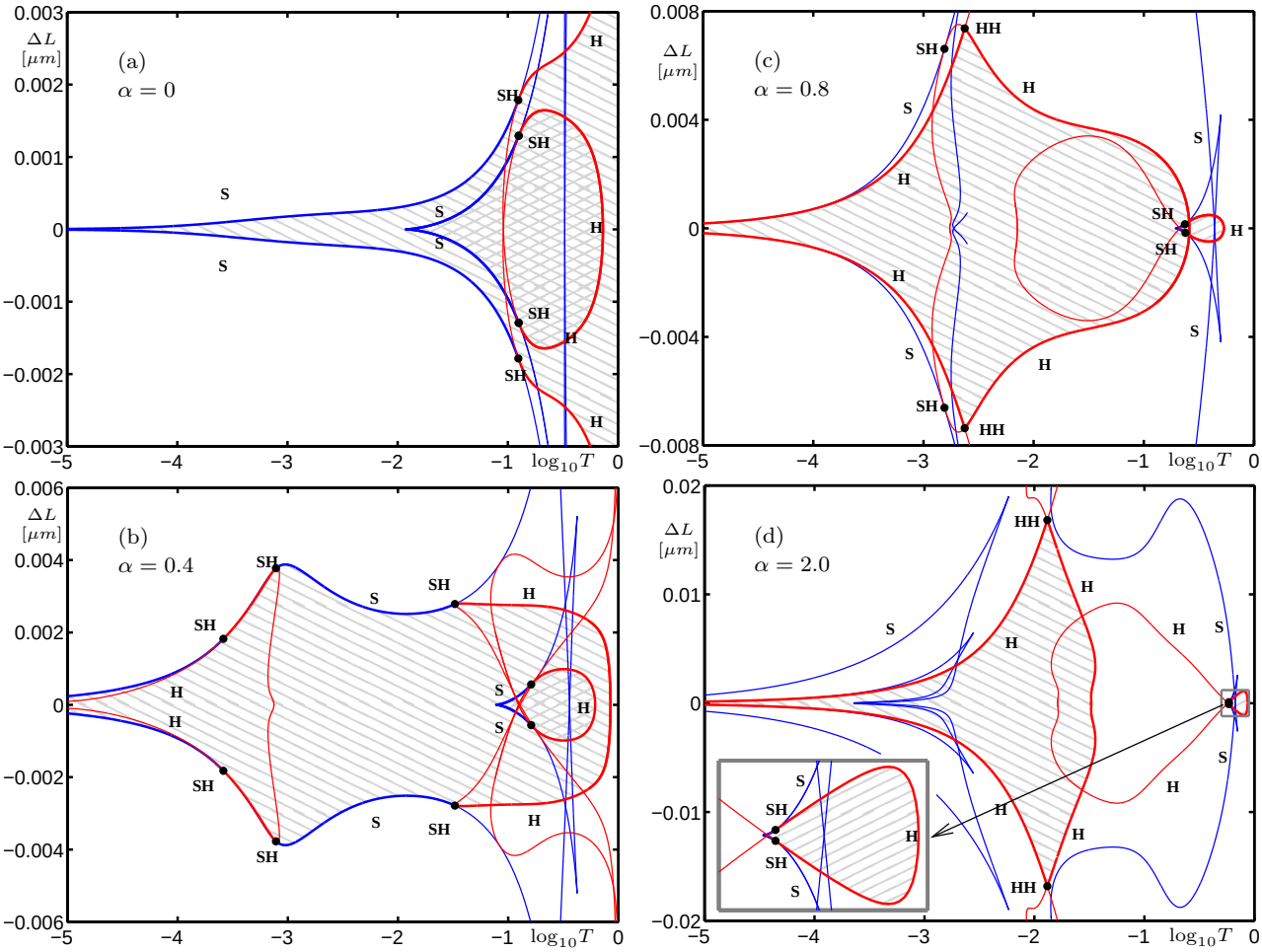

FIG. 9: (Color online) Bifurcation diagrams in the $(T, \Delta L)$ plane for different values of α and fixed gap size $L_G = 35\mu$m. Left inclined hatching indicates cw-operation in mode 2, right inclined hatching cw-operation of mode 1, crossed hatching bistability of both modes. Curves are saddle-node (S) and Hopf (H) bifurcations; black dots are codimension-two saddle-node Hopf (SH) and double Hopf (HH) points. The inset shows a enlarged view around certain codimension-two bifurcations as indicated by the arrow.

As α is increased to $\alpha = 0.4$ [Fig. 9(b)], the locking region dominated by composite-cavity mode 2 expands, whereas the locking region dominated by composite-cavity mode 1 shrinks and moves toward larger T. In addition, there appears an additional Hopf curve which becomes a part of the locking boundary at around $T = 10^{-3.5}$. This happens via codimension-three bifurcations where the additional Hopf curve becomes tangent to each of the two saddle-node curves at two points at $\Delta L \sim \pm 0.003$. After the bifurcation, one finds two additional pairs of saddle-node Hopf (SH) points indicating the change in the type of the locking boundary.

When α is increased to $\alpha = 0.8$ [Fig. 9(c)], the locking region dominated by the symmetric composite-cavity mode 2 expands noticeably in ΔL and moves to smaller T (weaker laser coupling). This expansion is a result of codimension-three bifurcations where two saddle-node-Hopf points (SH) meet and a double Hopf point (HH) emerges on the locking boundary. Here, this bifurcation involves the SH-points at $T = 10^{-1.5}$ in panel (b) that have moved to the left and the SH-points at $T = 10^{-3}$ in panel (b) that have moved to the right along the saddle node curves. Moreover, the SH-points at $T = 10^{-3.6}$ in panel (b) moved towards smaller T and left the parameter region displayed in Fig. 9(c). The locking region dominated by the anti-symmetric composite-cavity mode 1 remained unchanged but the bistability region shrank as the right- and left-inclined hatching regions started to separate.

Figure. 9(d) shows the bifurcation diagram for $\alpha = 2$ with two monostable locking regions. The much larger locking region dominated by the symmetric composite-cavity mode 2 found at low to moderate laser coupling is bounded by two Hopf (H) curves. The small locking re-

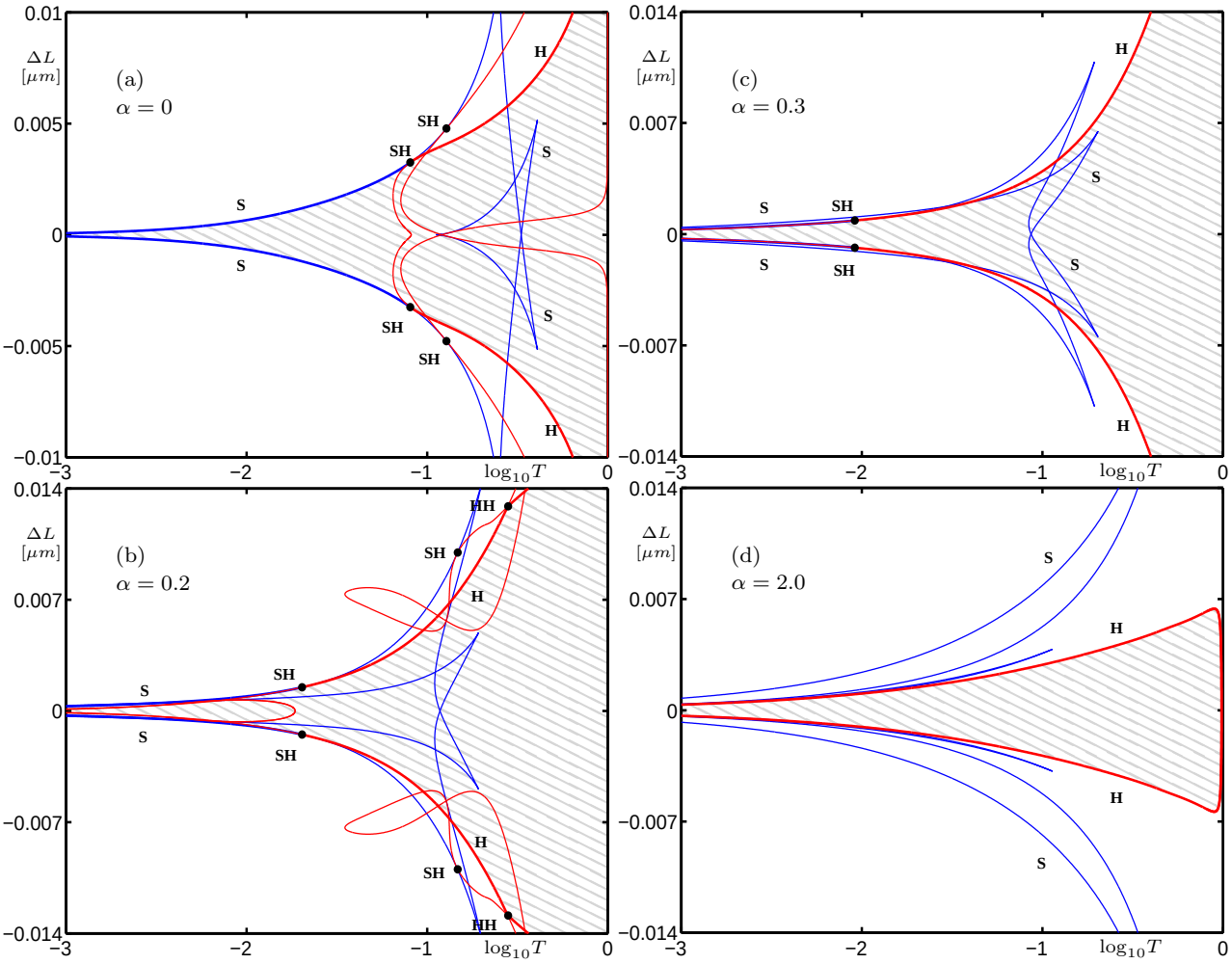

FIG. 10: (Color online) Bifurcation diagrams for in the $(T, \Delta L)$ plane for different values of α and fixed gap size $L_G = 280\mu$m. Left inclined hatching indicates cw-operation in mode 2, right inclined hatching cw-operation of mode 1, crossed hatching bistability of both modes. Curves are saddle-node (S) and Hopf (H) bifurcations. Black dots are codimension-two saddle-node Hopf (SH) and double Hopf (HH) points.

gion dominated by the anti-symmetric composite-cavity mode 1 found at strong laser coupling is bounded by saddle-node (SN) and Hopf (H) curves [inset in Fig. 9(d)].

In addition to a number of qualitative changes described, we would like to point out that the locking region expands significantly in the laser length difference ΔL with increasing α. This is consistent with the results obtained for an optically injected laser [15] and two lasers with instantaneous coupling [21, 45]. Interestingly, here the maximal expansion occurs at a transmission coefficient T that corresponds to weak/moderate laser coupling.

B. Large gap

Figure 10 shows the transformation of the locking region for $L_G = L_0 = 280\mu$m with increasing α. For $\alpha = 0$ [Fig 10(a)], there is a single and monostable locking region dominated by the symmetric composite-cavity mode 2 (left inclined) for all values of T. This result is the same as the result in Fig 5(d) with the locking region bounded by saddle-node (S) curves at small T and Hopf (H) curves at large T. As can be seen from Fig 10(b) for $\alpha = 0.2$, the locking region expands in ΔL. However, it does not move to smaller T and the maximal expansion occurs at largest T. Also, a double Hopf (HH) point emerges on the locking boundary. For $\alpha = 0.3$ [Fig. 10(c)] the double Hopf point moves outside of the frame and the locking boundary resembles the result from panel (a). When α is increased even further, the locking region shrinks slightly in ΔL and becomes bounded entirely by a single Hopf curve within the range shown in Fig. 10(d).

A comparison between Figs. 9 and 10 shows that the overall structure of the locking region is less dependent on

α when the length of the passive resonator is comparable to the length of the lasers.

V. BEYOND LOCKING

Modern applications of lasers in secure communication schemes, ultra-sensitive detectors, and random number generators require chaos rather than stable continuous wave emission [7, 50, 51]. In this context it is important to identify chaotic dynamics that is persistent or robust [52] with respect to fluctuations or drift in the system parameters. The stability analysis of the locked solutions in the previous sections revealed several codimension-two and three bifurcation points at the locking boundary. It is known from bifurcation theory [53] that such points can give rise to complicated dynamics including quasi-periodic and chaotic intensity oscillations and they were indeed found in Fig. 7.

The aim of this section is to uncover regions of chaotic dynamics in the $(T, \Delta L)$ plane. A detailed bifurcation analysis of periodic intensity oscillations would identify transitions to chaos and indicate parameter regions with chaotic dynamics, but it is technically difficult for complicated models such as Eqs. (3)–(4). An easier method to map out regions of chaos is the recently proposed 0-1 test for chaos [41]. This fast and easy to implement tool for time series analysis requires information about just one dynamical variable and gives a result of 1 for chaos and 0 for all other types of dynamics (equilibrium, periodic and quasi-periodic oscillations). In particular, it can facilitate experimental verification of chaos where one has typically access to only a few out of many dynamical variables.

To apply the test, the $(T, \Delta L)$ plane is covered with a grid of 800×600 points. For each grid point the time series of the population inversion N_B in laser B is obtained from time integration of Eqs. (3)–(4) and then tested for chaos [41]. Figure 11 shows the regions of chaotic dynamics in black for $\alpha = 2$ and three different sizes of the gap L_G. For reference, we also included hatched regions of stable locking. In the remaining white parameter regions the dynamics is either periodic or quasi-periodic. For small gap size $L_G = 5\mu$m [Fig. 11(a)] there are two distinct regions of chaotic dynamics. The larger region is found for $10^{-5} < T < 10^{-3}$ (weak coupling) and has distinguishable windows of periodic or quasi-periodic dynamics indicated by the white patches. The smaller region is found at strong coupling and non-zero detuning ΔL and has noticeably smaller windows of periodic or quasiperiodic dynamics. These two regions of chaotic dynamics are separated by the locking region at intermediate values of the transmission coefficient T. As this locking region shrinks in size with increasing L_G, the two regions of chaotic dynamics move to stronger laser coupling (larger T) and merge [Fig. 11(b)]. As L_G is increased further, the chaotic regions also shrink [Fig. 11(c)] and eventually disappear completely for $L_G \sim 50\mu$m. These

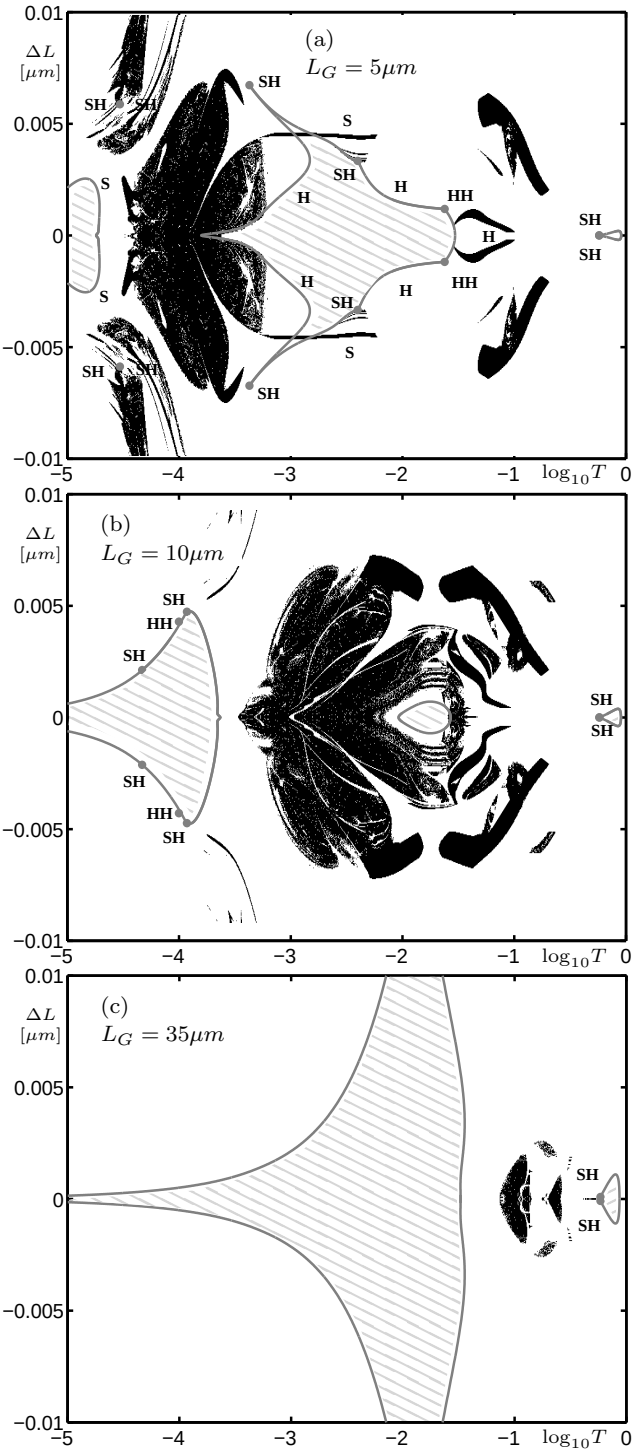

FIG. 11: Chaotic regions (black) in the $(T, \Delta L)$ plane for $\alpha = 2$ and different sizes of the gap L_G as indicated in the panels. Hatched areas indicate stable locking and bifurcation curves are in gray. Compare with Figs. 6(a), 6(b), and 9(f).

results are consistent with the bifurcation analysis of locked solutions in Fig. 6 showing that the codimension-two points also disappear from the parameter region considered with increasing L_G.

VI. DISCUSSION AND CONCLUSIONS

We studied the stability of two face-to-face coupled lasers that are spatially separated by a passive resonator, in terms of three interacting composite-cavity modes. The focus was on the effects of the passive resonator whose length ranged from much shorter than to comparable to the laser length. In this way, our results link the simpler problem of two instantaneously coupled lasers involving two composite-cavity modes and the more complicated problem of delay-coupled lasers involving a multitude of composite-cavity modes.

The analysis of the non-interacting composite-cavity modes already revealed interesting effects of the laser length difference ΔL, the transmission coefficient T of the coupling mirrors, and the length of the passive resonator L_G. On the one hand, we found strongly nonlinear dependence on T and ΔL of the composite-cavity mode overlap integrals which quantify modal gain, population-induced refractive index change, and coupling between the modes. On the other hand, we found strongly nonlinear dependence of the composite-cavity mode frequencies on the passive resonator length. In particular, the value of the transmission coefficient T at which all three composite-cavity modes come close to a resonance varies strongly with L_G. We considered the interaction of two anti-symmetric composite-cavity modes describing out-of-phase laser emission and one symmetric composite-cavity mode describing in-phase laser emission. Changing the length of the coupled-laser system by half of a wavelength would result in the interaction of two symmetric and one anti-symmetric composite-cavity mode.

The bifurcation analysis of nonlinear interactions between the three composite-cavity modes revealed a complicated structure of the stable locking regions in the $(T, \Delta L)$ plane. For zero amplitude-phase coupling of the electric field ($\alpha = 0$), we found a single uninterrupted locking region that is bistable for short passive resonators and monostable for passive resonators comparable in length to the lasers. For nonzero amplitude-phase coupling of the electric field ($\alpha = 2$), we found three separate and monostable locking regions that transform into a single monostable locking region via special codimension-three bifurcations as the passive resonator length is increased to the value comparable to the length of the lasers. The locking regions are typically dominated by one composite-cavity mode with all other modes having negligible amplitudes. On the one hand, our results for short compared to the lasers passive resonators are qualitatively similar to the instantaneous coupling model (no passive resonator) discussed in Ref. [44, 45] reporting a single bistable locking region for $\alpha = 0$ and two separate monostable locking regions for $\alpha = 2$. On the other hand, the effect reported here of a successive alternation between in-phase and out-of-phase locking with changing the length of the coupled-laser system in half wavelength steps relates to the in-phase and out-of-phase modes found in delay-coupled laser models [25, 27]. Finally, analysis of irregular intensity oscillations using the recently developed 0-1 test for chaos revealed an intricate structure of chaotic regions in the $(T, \Delta L)$ plane. The large regions of chaos found when the passive resonator is much shorter than the lasers shrink and eventually disappear as the passive resonator length increases.

The analysis presented here is a starting point for studying effects of more complicated passive structures, such as a photonic lattice, or optical nonlinearities in coupled-laser systems.

Acknowledgments

This research was supported by Great Western Research Grant No. 18 under "Modeling and nonlinear dynamics of optical nanodevices: nanolasers and photonic nanocircuits."

[1] H. Haken, Physics Letters A **53**, 77 (1975).
[2] D. Botez and D. Scifres, eds., *Diode Laser Arrays* (Cambridge University Press, 1994).
[3] J. Joannopoulos, R. Meade, and J. Winn, *Photonic Crystals: Molding the Flow of Light* (Princeton University Press, 1995).
[4] A. J. Danner, J. J. Raftery Jr., N. Yokouchi, and K. D. Choquette, Applied Physics Letters **84**, 1031 (2004).
[5] S. V. Zhukovsky, D. N. Chigrin, and J. Kroha, Physical Review A **79**, 033803 (pages 15) (2009).
[6] M. T. Hill, H. J. S. Dorren, T. de Vries, X. J. M. Leijtens, J. H. den Besten, B. Smalbrugge, Y. Oei, H. Binsma, G. Khoe, and M. K. Smit, Nature **432**, 206 (2004).
[7] A. Uchida, K. Amano, M. Inoue, K. Hirano, S. Naito, H. Someya, I. Oowada, T. Kurashige, M. Shiki, S. Yoshimori, et al., Nature Photonics **2**, 728 (2008).
[8] J. R. Terry, K. S. Thornburg, D. J. DeShazer, G. D. VanWiggeren, S. Zhu, P. Ashwin, and R. Roy, Phys. Rev. E **59**, 4036 (1999).
[9] F. Rogister and R. Roy, Physical Review Letters **98**, 104101 (pages 4) (2007).
[10] S. Riyopoulos, Phys. Rev. A **66**, 053820 (2002).
[11] R. Vicente, I. Fischer, and C. R. Mirasso, Physical Review E (Statistical, Nonlinear, and Soft Matter Physics) **78**, 066202 (pages 11) (2008).
[12] G. V. der Sande, M. C. Soriano, I. Fischer, and C. R. Mirasso, Physical Review E **77**, 055202 (pages 4) (2008).
[13] M. Spencer and J. W.E. Lamb, Phys. Rev. A **5**, 884

(1972).
[14] R. Lang, IEEE J. Quantum Electron. **QE-18**, 976 (1982).
[15] S. Wieczorek, B. Krauskopf, T. Simpson, and D. Lenstra, Physics Reports **416**, 1 (2005), ISSN 0370-1573.
[16] S. S. Wang and H. G. Winful, Applied Physics Letters **52**, 1774 (1988).
[17] P. Mandel, L. Ruo-ding, and T. Erneux, Phys. Rev. A **39**, 2502 (1989).
[18] H. G. Winful and L. Rahman, Phys. Rev. Lett. **65**, 1575 (1990).
[19] P. Ashwin, J. R. Terry, K. S. Thornburg, and R. Roy, Phys. Rev. E **58**, 7186 (1998).
[20] S. Yanchuk, K. R. Schneider, and L. Recke, Physical Review E (Statistical, Nonlinear, and Soft Matter Physics) **69**, 056221 (pages 12) (2004).
[21] S. Wieczorek and W. W. Chow, Physical Review A (Atomic, Molecular, and Optical Physics) **69**, 033811 (pages 17) (2004).
[22] R. Lang and K. Kobayashi, IEEE J. Quantum Electron. **QE-16**, 347 (1980).
[23] J. Mulet, C. Masoller, and C. R. Mirasso, Phys. Rev. A **65**, 063815 (2002).
[24] J. Javaloyes, P. Mandel, and D. Pieroux, Phys. Rev. E **67**, 036201 (2003).
[25] H. Erzgräber, D. Lenstra, B. Krauskopf, E. Wille, M. Peil, I. Fischer, and W. Elsäßer, Opt. Commun. **255(4-6)**, 286 (2005).
[26] H.-J. Wünsche, S. Bauer, J. Kreissl, O. Ushakov, N. Korneyev, F. Henneberger, E. Wille, H. Erzgräber, M. Peil, W. Elsäßer, et al., Phys. Rev. Lett. **94**, 163901 (2005).
[27] H. Erzgräber, B. Krauskopf, and D. Lenstra, SIAM J. Appl. Dyn. Syst. **5**, 30 (2006).
[28] H. Erzgräber, E. Wille, B. Krauskopf, and I. Fischer, Nonlinearity **22**, 585 (2009).
[29] M. Yousefi and D. Lenstra, Quantum Electronics, IEEE Journal of **35**, 970 (1999), ISSN 0018-9197.
[30] S. Schikora, P. Hövel, H.-J. Wünsche, E. Schöll, and F. Henneberger, Physical Review Letters **97**, 213902 (pages 4) (2006).
[31] H. Erzgräber, B. Krauskopf, and D. Lenstra, SIAM Journal on Applied Dynamical Systems **6**, 1 (2007).
[32] O. V. Ushakov, H.-J. Wünsche, F. Henneberger, I. A. Khovanov, L. Schimansky-Geier, and M. A. Zaks, Phys. Rev. Lett. **95**, 123903 (2005).
[33] M. Radziunas and H.-J. Wünsche, *in Optoelectronic Devices, (J. Piprek ed.)* (Springer, New York, 2005), pp. 121–150.
[34] O. Hess, *in B. Krauskopf and D. Lenstra (eds.) Fundamental Issues of Nonlinear Laser Dynamics* (American Institute of Physics, 2000), vol. 548 of *AIP Conference Proceedings*, chap. Theory and Simulation of Spatially Extended Semiconductor Lasers, pp. 128–148.
[35] C. R. Mirasso, M. Kolesik, M. Matus, J. K. White, and J. V. Moloney, Phys. Rev. A **65**, 013805 (2001).
[36] J. Sieber, SIAM Journal on Applied Dynamical Systems **1**, 248 (2002).
[37] S. A. Shakir and W. W. Chow, Opt. Lett. **9**, 202 (1984).
[38] E. Kapon and J. Katz, Opt. Lett. **9**, 125 (1984).
[39] E. Doedel, A. Champneys, T. Fairgieve, Y. Kuznetsov, B. Oldeman, R. Paffenroth, B. Sandstede, X. Wang, and C. Zhang, Tech. Rep., Concordia University, Montreal, Canada (2007).
[40] G. A. Gottwald and I. Melbourne (A new test for chaos in deterministic systems), Proc. R. Soc. Lond. A **460**, 603 (2004).
[41] G. A. Gottwald and I. Melbourne, Physica D: Nonlinear Phenomena **212**, 100 (2005), ISSN 0167-2789.
[42] G. A. Gottwald and I. Melbourne, SIAM Journal on Applied Dynamical Systems **8**, 129 (2009).
[43] S. A. Shakir and W. W. Chow, Phys. Rev. A **32**, 983 (1985).
[44] W. W. Chow, IEEE J. Quantum Electron. **QE-22(8)**, 1174 (1986).
[45] S. Wieczorek and W. W. Chow, Optics Communications **246**, 471 (2005).
[46] C. H. Henry, IEEE J. Quantum Electron. **18**, 259 (1982).
[47] W. W. Chow, Physical Review A (Atomic, Molecular, and Optical Physics) **73**, 013821 (pages 9) (2006).
[48] M. Sargent III, M. Scully, and W. Lamb, *Laser Physics* (Addison-Wesley, New York, 1974).
[49] W. W. Chow, S. W. Koch, and M. Sargent III, *Semiconductor Laser Physics* (Springer Verlag, Berlin, 1997).
[50] G. D. VanWiggeren and R. Roy, Science **279**, 1198 (1998).
[51] W. W.Chow and S. Wieczorek, Optics Express **17**, 7491 (2009).
[52] D. J. Albers, J. C. Sprott, and J. P. Crutchfield, Physical Review E **74**, 057201 (pages 4) (2006).
[53] Y. Kuznetsov, *Elements of Applied Bifurcation Thory* (Springer, 2004).